



Synthesis, structure and electro-chemical characterization of complex perovskites, Ba_2MTaO_6 ($M = \text{Ce}, \text{Pr}$) and $\text{Ba}_3\text{Pr}_x\text{Ta}_y\text{O}_{9-\delta}$ ($x = 1, 2$; $y = 1, 2$)

Master's thesis in Chemistry and Chemical Engineering

XUNCHENG SHI



Synthesis, structure and electrochemical characterization of complex perovskites,

Ba_2MTaO_6 ($M = \text{Ce}, \text{Pr}$) and $\text{Ba}_3\text{Pr}_x\text{Ta}_y\text{O}_{9-\delta}$ ($x = 1, 2; y = 1, 2$)

XUNCHENG SHI

Synthesis, structure and electrochemical characterization of complex perovskites,
 Ba_2MTaO_6 ($M = \text{Ce}, \text{Pr}$) and $\text{Ba}_3\text{Pr}_x\text{Ta}_y\text{O}_{9-\delta}$ ($x = 1, 2; y = 1, 2$)

XUNCHENG SHI

© XUNCHENG SHI, 2018.

Supervisors: Seikh M. H. Rahman, Dariusz W. Wardecki, Paul F. Henry

Examiner: Jan-Erik Svensson

Department of Chemistry and Chemical Engineering

Chalmers University of Technology

SE-412 96 Göteborg

Sweden

Telephone + 46 (0)31-772 1000

Synthesis, structure and electrochemical characterization of complex perovskites, Ba_2MTaO_6 ($M = \text{Ce}, \text{Pr}$) and $\text{Ba}_3\text{Pr}_x\text{Ta}_y\text{O}_{9-\delta}$ ($x = 1, 2; y = 1, 2$)

XUNCHENG SHI

Department of Chemistry and Chemical Engineering

Chalmers University of Technology

ABSTRACT

Five samples of complex perovskites Ba_2MTaO_6 ($M = \text{Ce}, \text{Pr}$) and $\text{Ba}_3\text{Pr}_x\text{Ta}_y\text{O}_{9-\delta}$ ($x = 1, 2; y = 1, 2$) were studied for use in the intermediate temperature proton conducting fuel cells (IT-PCFC). Samples were prepared by solid state synthesis method and their purity was checked by X-ray powder diffraction (XRPD). Phases $\text{Ba}_2\text{CeTaO}_6$, $\text{Ba}_2\text{PrTaO}_6$ and $\text{Ba}_3\text{PrTaO}_{9-\delta}$ were proved to be pure. The accurate chemical formula of the samples was carried out by energy dispersive spectroscopy (EDS). Rietveld refinement on XRPD data was used to confirm the purity and chemical formula of $\text{Ba}_2\text{CeTaO}_6$ and $\text{Ba}_3\text{PrTaO}_{9-\delta}$. Additionally, Rietveld refinement of $\text{Ba}_2\text{PrTaO}_6$ based on neutron powder diffraction data was used as a complementary method to the XRPD and EDS results and allowed for the crystal structure characterization. $\text{Ba}_3\text{PrTaO}_{9-\delta}$ is a new material and its synthesis and characterization have been described for the first time in this thesis. The conductivity of $\text{Ba}_2\text{CeTaO}_6$, $\text{Ba}_2\text{PrTaO}_6$, and $\text{Ba}_3\text{PrTaO}_{9-\delta}$ was measured by using electrochemical impedance spectroscopy (EIS). Thermogravimetric analysis (TG) and differential scanning calorimetry (DSC) data was used to study the dehydration process for pre-hydrated $\text{Ba}_2\text{CeTaO}_6$ and $\text{Ba}_2\text{PrTaO}_6$ samples. It was combined with the EIS results to study the oxygen vacancies. $\text{Ba}_2\text{PrTaO}_6$ showed a good mixed conductivity which makes this material a good candidate for the cathode material in PCFC.

Keywords: Double perovskite, complex perovskite, X-ray powder diffraction, neutron powder diffraction, Rietveld refinement, Electrochemical Impedance, proton conductivity, electronic conductivity.

Acknowledgements

I would like to show my deepest gratitude to my supervisors, Dr. Seikh M. H. Rahman, Researcher at Department of Chemistry and Chemical Engineering, Chalmers University of Technology, Gothenburg, Sweden and Dr. Dariusz W. Wardecki, Post Doc at Department of Chemistry and Chemical Engineering, Chalmers University of Technology, Gothenburg, Sweden for their unlimited guidance, ideas, and valuable suggestions on my research work and their support to relax myself outside the work. I would also like to thank my co-supervisor, Prof. Paul F. Henry, Adjunct Professor at Department of Chemistry and Chemical Engineering, Chalmers University of Technology, Gothenburg, Sweden for his valuable suggestions.

I would like to thank Prof. Sten G. Eriksson for giving me the opportunity to do my master thesis at his oxide group, as well as providing me a good condition focusing on the research without worrying about anything else than the research, and unconditional guidance on my writing. Many thanks to Nico Torino for the useful discussion and suggestion about the problems I met during the research.

The ISIS Facility, Rutherford Appleton Laboratory is thanked for rapid access to neutron beam facilities (experiment HRPD Xpress 1790227, 1790229 and 1790230). We thank Dr. Dominic Fortes at the HRPD beamline for performing neutron diffraction measurements.

I am grateful to my examiner Prof. Jan-Erik Svensson and thankful to all the colleagues in OOMK division for the support and friendship.

Finally, I would like to thank my parents and my brother Yan Hao for their unconditional support.

Table of Contents

1	Introduction	1
1.1	Background and Motivation	1
1.2	Perovskite	4
1.2.1	Double Perovskite	5
1.2.2	Ordering 1:1	6
1.2.3	Ordering 1:2	6
1.3	Protonic defect	7
1.3.1	Defect formation	7
1.3.2	Transport of protonic defects	8
2	Experimental Techniques	9
2.1	Preparation	9
2.1.1	Solid state synthesis	9
2.1.2	Vacuum drying	10
2.1.3	Hydration	10
2.2	Diffraction	11
2.2.1	X-ray powder diffraction	13
2.2.2	Neutron powder diffraction	13
2.2.3	The Rietveld method	14
2.3	Thermogravimetric analysis and differential scanning calorimetry	15
2.4	Scanning electron microscopy and Energy dispersive spectroscopy	16
2.5	Electrochemical impedance spectroscopy	17
3	Result and Discussion	21
3.1	Diffraction	21
3.2	Scanning electron microscopy and Energy dispersive spectroscopy	30
3.3	Thermogravimetric analysis and differential scanning calorimetry	33
3.4	Electrochemical characterization	34
4	Conclusion	38
5	Bibliography	39

List of Figures

Figure 1.1 Principle of (a) Solid oxide fuel cell and (b) Proton conducting fuel cell.	2
Figure 1.2 Cubic structure of the perovskite CaTiO_3 , where the Ca (green) located in the center, Ti (blue) located on each corner and O (red) located on the center of the edge.	4
Figure 1.3 Three types of sublattice: a) random, b) rock salt, c) layered perovskite).	5
Figure 1.4 Double perovskite structure of $\text{Sr}_2\text{MoFeO}_6$	6
Figure 1.5 Description of the Grotthuss mechanism [22].	7
Figure 2.1 Description of Bragg's Law. Constructive interference a) and destructive interference b) are shown.	12
Figure 2.2 A brief description of TG-DSC machine setup.	16
Figure 2.3 Representation of impedance on the complex plane.	17
Figure 2.4 Impedance plot of BPT at 400°C under dry and wet Ar condition including the fitting of semicircles based on the model of equivalent circuit.	18
Figure 2.5 Description of the cell setup used for the impedance measurements.	20
Figure 3.1 XRPD patterns of BCT synthesized at 1400°C and 1425°C	21
Figure 3.2 Rietveld refinement on XRPD for BCT.	22
Figure 3.3 XRPD patterns of BPT synthesized at 1300°C and 1350°C . The insert shows a better crystallinity for the sample annealed at 1350°C	25
Figure 3.4 Rietveld Refinement on HRPD data from the 168° detector bank for BPT.	25
Figure 3.5 Refined structure of BPT.	27
Figure 3.6 XRPD patterns of $\text{Ba}_3\text{Pr}_x\text{Ta}_y\text{O}_{9-\delta}$. The patterns are compared with a phase pure $\text{Ba}_2\text{PrTaO}_6$ to examine the purity.	29
Figure 3.7 Pattern matching of $\text{Ba}_3\text{PrTaO}_{9-\delta}$ using the Pawley method.	29
Figure 3.8 SEM micrograph of the BCT pellet.	31
Figure 3.9 SEM micrograph of the BPT pellet.	32
Figure 3.10 TG-DSC for hydrated BCT under inert atmosphere.	33
Figure 3.11 TG-DSC for hydrated BPT under inert atmosphere.	34
Figure 3.12 Arrhenius plot for the total conductivity of BCT measured under different conditions.	36
Figure 3.13 Arrhenius plot for the total conductivity of BPT measured under different conditions.	36
Figure 3.14 Arrhenius plot for the total conductivity of B3PT measured under different conditions.	37

List of abbreviations

AC	Alternating current
BCN18	$\text{Ba}_3\text{Ca}_{1.18}\text{Nb}_{1.82}\text{O}_{9-\delta}$
BCT	$\text{Ba}_2\text{CeTaO}_6$
BPT	$\text{Ba}_2\text{PrTaO}_6$
B3PT	$\text{Ba}_3\text{PrTaO}_{9-\delta}$
B3P2T	$\text{Ba}_3\text{Pr}_2\text{TaO}_{9-\delta}$
B3PT2	$\text{Ba}_3\text{PrTa}_2\text{O}_{9-\delta}$
CW	Constant wavelength
DSC	Differential scanning calorimetry
EDS	Energy dispersive X-ray Spectroscopy
EIS	Electrochemical Impedance Spectroscopy
HRPD	High-resolution powder diffractometer
ICDD	International centre for diffraction data
ICSD	Inorganic crystal structure database
MCFC	Molten carbonate fuel cell
NPD	Neutron powder diffraction
PAFC	Phosphoric acid fuel cell
PCFC	Proton conducting fuel cell
PEMFC	Proton exchange membrane fuel cell
SEM	Scanning electron microscopy
SOFC	Solid oxide fuel cell
TG	Thermogravimetric analysis
TOF	Time-of-flight
XRPD	X-ray powder diffraction

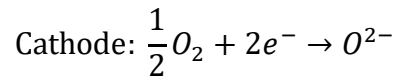
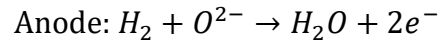
1 Introduction

1.1 Background and Motivation

The development of human civilisation is driven by accessing useful sources of energy. Since the industrial revolution, the fossil fuels have contributed to almost 80% of the energy consumption in the world. Today, the fossil fuels still dominate in over 60% of the energy market. To convert chemical energy stored in the fossil fuel into useful energy, combustion is the most widely used method. However, combustion has an extremely low efficiency. In an internal combustion engine, the entire efficiency reaches only about 20% to 30%. It also causes severe problems to the natural environment. The most ‘famous’ problem is the global warming, caused by the exhaust of carbon dioxide, nitrous oxide and methane from the combustion engine. To fulfil the Paris Agreement on COP21, it is important to find a sustainable alternative that satisfies the growing demand for energy [1, 2].

Unlike conventional sources based on the fossil fuels, fuel cells convert chemical energy directly into electric power, which results in a high efficiency and low emission [3]. When using H_2 and O_2 as fuel, water will be the only by-product, which makes it possible to generate fully clean energy. Depending on the electrolyte materials, there are four main kinds of fuel cells, proton exchange membrane fuel cells (PEMFCs), phosphoric acid fuel cells (PAFCs), solid oxide fuel cells (SOFCs), and molten carbonate fuel cells (MCFCs). [3, 4] Among them, SOFCs receive lots of interest, due to their high efficiency, usage of solid oxide electrolyte that avoid the risk of electrolyte leakage and corrosion, and broad choices of fuels.

In SOFCs, as shown in Figure 1.1a, oxygen ions migrate from cathode to anode through the electrolyte and react with hydrogen gas to form water and electrons, which supply the outer electric circuit. In this process, H_2 and O_2 are fed as a fuel. During the electrochemical reaction, heat and electricity is generated. The reactions are performed as [5-7]:



According to Fabbri's summary [3, 8], the current SOFCs are mainly built up using the yttria-stabilized zirconia electrolytes [9]. In order to have a good conductivity and minimize the ohmic loss, this setup requires a working temperature around 800 °C to 1000 °C. As such high working temperature, several disadvantages start to occur. A long starting time for heating up is needed. Moreover, a large amount of energy is required to keep the SOFC working at the operating temperature. Expensive materials are needed to withstand the corrosion of other SOFC parts at high temperature. These are the main reasons that limit the SOFCs to be brought into commercial use. Further investigations to lower the operating temperature of SOFCs are necessary. The optimal temperature range for SOFCs was set by Steele in 2001 to be from 400 °C to 700 °C [10, 11].

Lots of challenges occur when building up a system for intermediate temperature SOFC. One of them is to find a proper electrolyte that has better conductivity than commonly used yttria-stabilized zirconia around 400 °C to 700 °C. In this case, proton conductors can be a good alternative. In 1981, Iwahara reported the proton conductivity in oxide materials under humid atmosphere above 600 °C [12]. Later in 1993, Liang and Nowick confirmed the proton conductivity in mixed perovskite oxide materials [13]. In 1996, a famous complex perovskite material, with protons as conducting ions, $Ba_3Ca_{1.18}Nb_{1.82}O_{9.8}$, was reported by Yang and

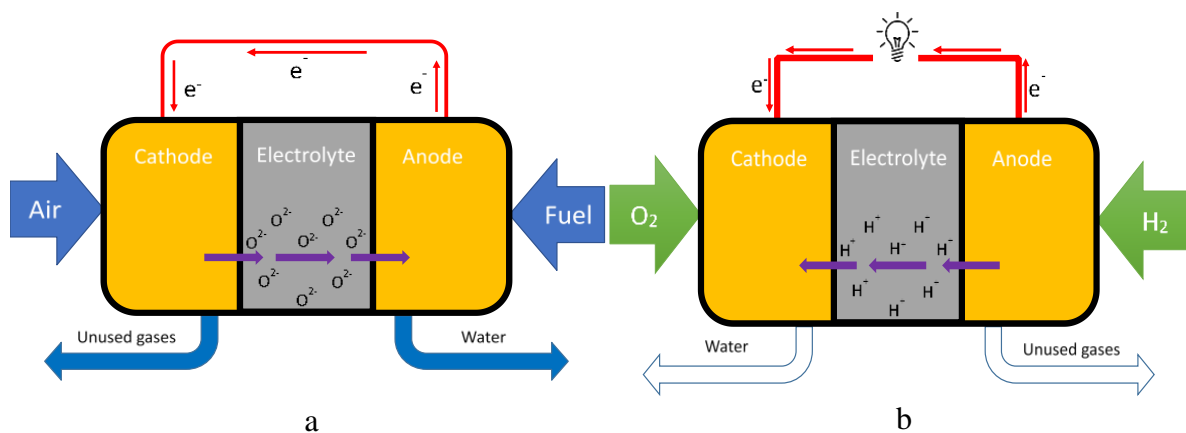
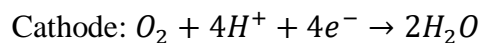
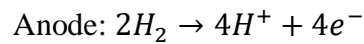


Figure 1.1 Principle of (a) Solid oxide fuel cell and (b) Proton conducting fuel cell.

Nowick to have good proton conductivity [14]. Figure 1.1b shows a scheme of the proton conducting fuel cells (PCFCs). In this type of the fuel cell, protons migrate from anode to cathode and react with oxygen gas to form water. Electrons that power the outer circuit are obtained when a H₂ molecule is split into protons. The reaction is as follows:



Hydrogen gas is oxidized into protons on the anode. The protons diffuse through the electrolyte to the cathode and form reduction reaction with oxygen and the electrons coming back through the outer electric circuit. Compared to the materials used for SOFCs, materials in PCFCs require a lower activation energy. Protons have a much smaller radius as compared with the oxide-ion, which makes them easier to transfer between the crystal lattice defects. Formation of water on the cathode side instead of anode side is also beneficial and it avoids fuel dilution [3, 8].

In PCFCs, the cathode material is also a big challenge especially at intermediate temperature (400 °C to 700 °C). The anode reaction is less dependant on the temperature, which indicates a fast kinetics on the anode side [11]. However, due to the decrease in temperature, proton conductivity will decline. For pure proton conductors, the cathode reaction is limited only to the interface between cathode and electrolyte, which results in slow kinetics and a polarization loss [3]. In order to increase the kinetics of the cathode reaction and lower the polarization loss, materials used in cathodes need to have a good mixed proton and electronic conductivity.

Bhella has reported good total conductivity of $6.1 \times 10^{-4} \text{ Scm}^{-1}$ in $Ba_2(Ca_{0.79}Nb_{0.66}Ta_{0.55})O_{6-\delta}$ at 650°C [15]. Fabbri has reported good total conductivity of $6 \times 10^{-3} \text{ Scm}^{-1}$ at 450°C in $BaZr_{0.7}Pr_{0.1}Y_{0.2}O_{3-\delta}$ [16]. Furuichi reported good ion conductivity in $BaPrO_{3-\delta}$ which can be a good candidate for the anode material in SOFC [17]. In 2006, Haugrud and Norby reported the presence of mixed protonic, native ionic and electronic conductivity in $RE_{1-x}A_xMO_4$ (RE =rare-earth elements; A =Ba, Ca, Sr; M =Nb, Ta) [18].

The purpose for this study is to find materials that have an improved conductivity for electrolyte or electrode in PCFC. The studied materials come from a group of perovskites.

1.2 Perovskite

The perovskite structure has a chemical formula of ABO_3 . As an example, Figure 1.2 shows a cubic structure of $CaTiO_3$. In the structure, the atoms occupy the following positions, Ca^{2+} is located at the center of the unit cell ($\frac{1}{2}, \frac{1}{2}, \frac{1}{2}$); Ti^{4+} occupies a position (0, 0, 0); and O^{2-} is located in the middle of the edge at positions ($\frac{1}{2}, 0, 0$), (0, $\frac{1}{2}, 0$) and (0, 0, $\frac{1}{2}$). Each Ca^{2+} is coordinated by 12 O^{2-} and Ti^{4+} is coordinated by six O^{2-} [7].

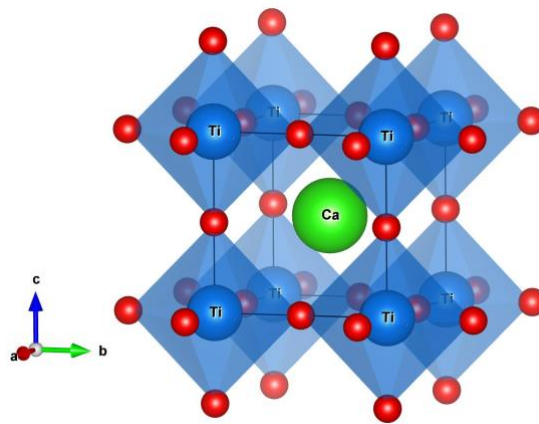


Figure 1.2 Cubic structure of the perovskite $CaTiO_3$, where the Ca (green) located in the center, Ti (blue) located on each corner and O (red) located on the center of the edge.

The actual structure of the perovskites is influenced by the size of cations and anions. It can be predicted by the so-called tolerance factor t using the equation [19, 20]:

$$t = \frac{r_A + r_O}{\sqrt{2}(r_B + r_O)}, \quad (1)$$

where the r_A and r_B are the ionic radii for the A -atom and B -atoms, respectively, and r_O is the O^{2-} radius. In general, the perovskite structure will have the parameter t around 0.89 to 1.06 [5, 6]. With decreasing t , the more distortions will be present in the structure.

1.2.1 Double Perovskite

Substitution of some atomic sites in the perovskite structure are possible. It can take place on either *A* or *B* site, or both, with different atoms in different ratio. A structure formed as $AA'BB'O_3$ are known as complex perovskites [7]. In double perovskites which belong to a subgroup of the complex perovskites, the substitution will only happen on either *A* or *B* site. That forms a chemical formula as $A_2BB'O_6$, $[A(BB')O_3]$ or $AA'B''O_3$ etcetera. [5]. The unit cell is doubled in each direction as compared with a single perovskite structure (shown in Figure 1.4). There will be two different atoms located on the *B* site and their coordination remains the same as in a single perovskite structure [21].

The physical properties are mainly defined by the arrangement of atoms at the *B* site in a sublattice. There are three different arrangement [5] of the sublattice shown in Figure 1.3.

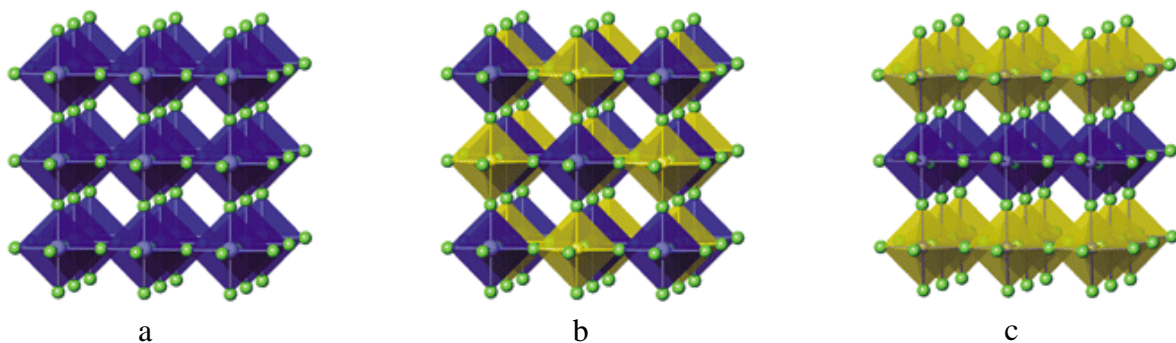


Figure 1.3 Three types of sublattice: a) random, b) rock salt, c) layered perovskite).

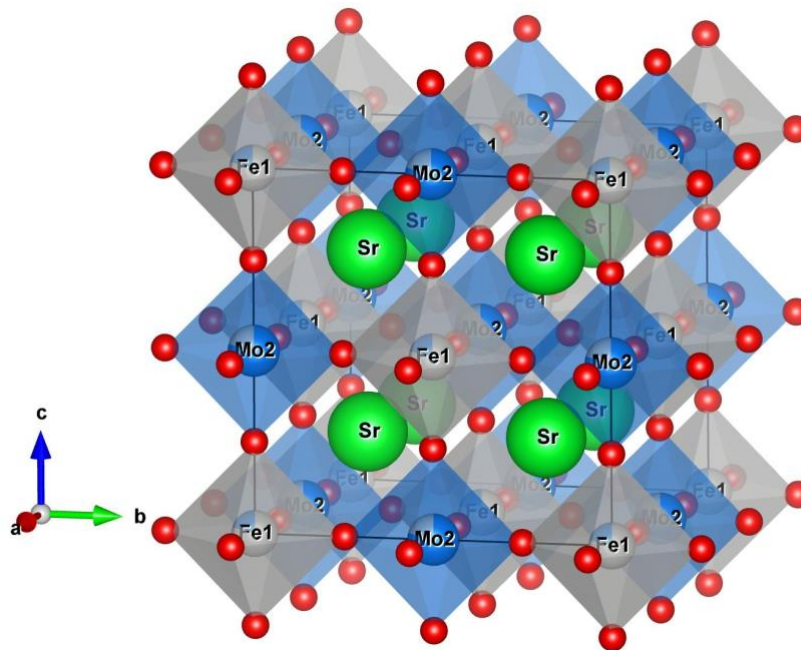


Figure 1.4 Double perovskite structure of $\text{Sr}_2\text{MoFeO}_6$.

1.2.2 Ordering 1:1

The 1:1 ordered double perovskite has a formula of $A_2BB'O_6$ [5]. The A cation should have a charge of 2+. However, the valence of B and B' can be varied. Combinations of 3+ and 5+ cations, 2+ and 6+ cations or two 4+ cations are all possible to be placed on the B site. In general, the average B site valance should be 4+ [6]. Because the B and B' all go to the B site with a 1:1 ratio, the arrangement of B site in the sublattice for double perovskite is of rock salt type, which is shown in Figure 1.4. This is so-called an ordered double perovskite.

1.2.3 Ordering 1:2

The 1:2 ordered double perovskite has a formula of $A_3BB'_2O_9$ [5]. As in the 1:1 ordered double perovskite, the A cation will still have a charge of 2+. However, charges on the B site can show lots of combinations. In general, the average valence on B site should be 4+.

1.3 Protonic defect

1.3.1 Defect formation

A proton, due to its small radius, cannot occupy any interstitial site in the crystal structure. To form protonic defects, protons need to interact with the O^{2-} ion in the structure to form hydroxide (OH^-) [7]. If there is an oxygen vacancy in the structure it will be filled by hydroxide ion. Here the hydroxide ion and proton are provided by the hydrolysis of water. This indicates that the concentration of protonic defect is related to the number of oxygen vacancies in the crystal lattice. Changing the ratio of the elements at the *A* or *B* sites can lead to increased number of oxygen vacancies [6]. Vacancies created in this way is an intrinsic defect where no external elements are involved.

However, introducing external elements, such as by doping, oxygen vacancies can also form [6]. In an ordered double perovskite, *A* site should have an ion charge for $2+$ and *B* site should have an average charge of $4+$. However, doping on either *A* site or *B* site with a lower valence ion will introduce a charge compensation, which makes it possible to create oxygen vacancies.

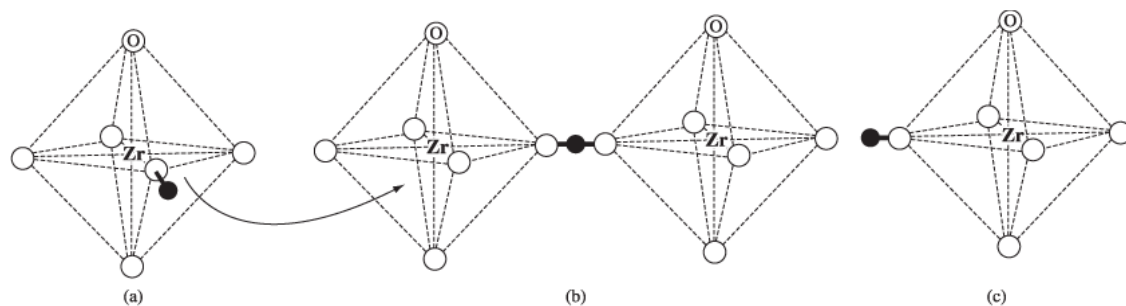
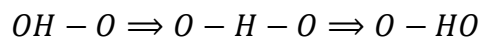


Figure 1.5 Description of the Grotthuss mechanism [22].

1.3.2 Transport of protonic defects

There are two models explaining the proton transport in the perovskite materials. The Grotthuss mechanism [20], shown in

Figure 1.5, describes protons that are first transferred between the neighboring oxygen atoms inside the structure. Hydroxide ion on the oxygen site starts to reorient and jumps to the oxygen atoms on the neighboring octahedron. The overall migration can be written as:



The last step was considered as the rate-limiting step, where the activation energy in general is in the order of 0.4 eV to 0.6 eV [23].

Another mechanism is so called the Vehicle Mechanism [24]. The proton is embedded into H₂O molecule and form H₃O⁺. The H₃O⁺ transfers in liquid, in metals, or tunnel like structure.

2 Experimental Techniques

2.1 Preparation

2.1.1 Solid state synthesis

Solid state route is the simplest and the most common method for synthesizing oxide materials. In order to obtain the final product, stoichiometric amounts of starting reactants were mixed, ground in a mortar, and calcined at high temperature in a furnace. Diffusion between two nearby particles is the driving force in those reactions [7]. Therefore, a homogeneous mixture before calcination is one of the most important factors in this procedure. Moreover, a certain concentration of lattice defects is necessary for ion exchange during the reaction [25]. For those reason, the procedure was designed as follows:

Grinding- Pelletizing- Calcination

High temperature is essential in sold state synthesis in order to decrease the reaction time. Higher temperature will give higher diffusion rate, which will bring the reaction time into a reasonable range. However, if the particle size is reduced, which results in a higher surface-to-volume ratio, the energy for diffusion will be less [6]. Thus, the temperature needed will be lower. In general, the temperature should not go above the reactants' melting point.

In this study, BaCO₃ (Alfa Aesar[®], >99.8%), Pr₆O₁₁ (Aldrich[®], >99.9%), CeO₂ (G. Frederick Smith Chemical Co.[®], >99.9%) and Ta₂O₅ (Aldrich[®], >99%) were used as starting reactants. All the starting materials were mixed at certain ratio and ground with ethanol in an agate mortar. For the first calcination, the mixture was placed into a crucible and heated at 850 °C for 12 h in a box furnace (Entech Energiteknik AB[®], MF 2/15-SP).

Table 2.1 Description on each step for synthesis.

Sample	2 nd round, Temp./Dur.	3 rd round, Temp./Dur.
Ba ₂ CeTaO ₆ (BCT)	1400 °C/12 h, under H ₂ flux	1425 °C/20 h, under H ₂ flux
Ba ₂ PrTaO ₆ (BPT)	1300 °C/24 h	1350 °C/12 h
Ba ₃ PrTa ₂ O _{9-δ} (B3PT2)	1300 °C/24 h	1350 °C/12 h
Ba ₃ Pr ₂ TaO _{9-δ} (B3P2T)	1300 °C/24 h, under H ₂ flux	1350 °C/12 h, under H ₂ flux
Ba ₃ PrTaO _{9-δ} (B3PT)	1300 °C/24 h	1350 °C/12 h

After that, the mixture was ground again, pressed into a 13 mm-diameter pellet and heated at higher temperature in a tube furnace (Lenton Thermal Designs[®], LTF 16/25/450). All the crucibles used during the synthesis were made of alumina. This procedure was repeated until the sample was pure. In total, five samples were made, and they are listed in Table 2.1. Temperature and duration for each step is also shown in Table 2.1.

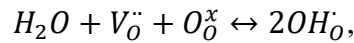
2.1.2 Vacuum drying

During synthesis, humidity from the atmosphere can fill the vacancies and form protonic defect. With that amount of undesired water in the structure, measurement on the amount of defect later will be affected. For this reason, it is important to remove water in advance. The sample was prepared in an alumina crucible and heated to 900 °C for 12 h in a tube furnace (Entech Energiteknik AB[®], ETF 40/15) with one side sealed and another side connected to a high vacuum pump (Edwards High Vacuum INT.[®], E2M1.5).

2.1.3 Hydration

Proton defects were incorporated into the sample structure through hydration process. While exposing under humid condition, the water molecules will be hydrolyzed into a proton and a hydroxide ion. The oxygen vacancies created during the synthesis will be filled by the

hydroxide ion and the proton will form covalent bond with the oxygen ion in the structure [6, 7]. Finally, two protonic defects are formed. Reaction using the Kröger-Vink notation is given as: [26]



where $V_O^{\cdot\cdot}$ stands for the oxygen vacancies with two negative charges on oxygen site in the structure. O_O^x stands for the neutral oxygen on oxygen site. OH_O^{\cdot} stands for the substantial hydroxyl on oxygen site. The sample was exposed under a humid Argon flow for several days (5-7 days). A thermogravimetric analysis was used to measure the temperature for hydration.

A furnace made by Vecstar[®], VCTF4, was used for Hydration.

2.2 Diffraction

Diffraction is one of the most commonly used experimental techniques to determine a crystal structure of materials as well as to check purity of samples. In this study, X-ray powder diffraction (XRPD) and neutron powder diffraction (NPD) methods were used.

Diffraction methods are based on the well-known physical phenomenon, wave interference [27]. Adding two waves which are in-phase, leads to the constructive interference whereas if they are added out-of-phase destructive interference occurs. A direction in space where the constructive interference occurs can be described by the diffraction angle 2θ . This angle is normally defined as an angle between direction of the incident wave and the direction of the diffracted wave. The nature of waves in the diffraction process is not crucial. They can be either electromagnetic waves including X-rays or matter waves like neutrons or electrons. [7, 25]

In 1913 L. Bragg and his father W. H. Bragg found a relation between diffraction angles 2θ and Miller indices (hkl) which describe crystallographic planes in a crystal [28]. Figure 2.1 shows a diffraction process on a selected set of crystallographic planes with defined d-spacing. The constructive interference will occur only when the diffracted waves are in-phase (Fig 2.1a). It happens when the following equation is satisfied:

$$n\lambda = 2d_{hkl} \sin \theta_{hkl} \quad (2)$$

where n is the integer, λ is the wavelength of the incident beam. This is the well-known Bragg's equation.

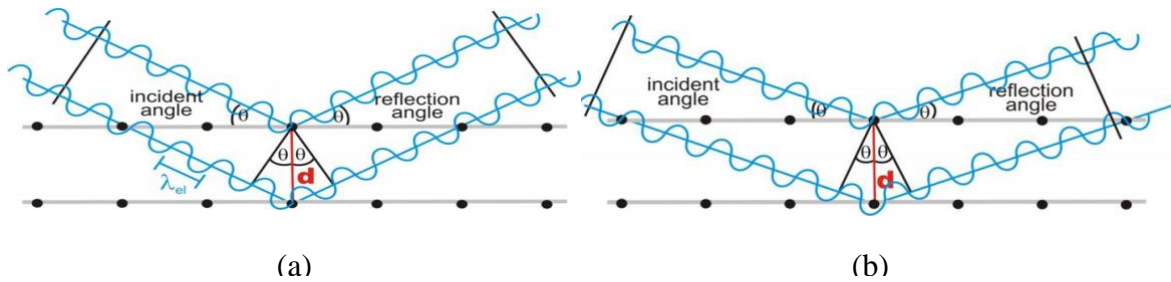


Figure 2.1 Description of Bragg's Law. Constructive interference a) and destructive interference b) are shown.

If the wavelength λ and the diffraction angle 2θ is known the d-spacing for different (hkl) planes can be calculated. [7, 29]

A result of the powder diffraction measurement is so called diffraction pattern which presents intensities (Bragg peaks) of the diffracted beam as a function of the diffraction angle 2θ . According to Eq. 2, positions 2θ of the Bragg peaks provide information about the d-spacing for different (hkl) planes and further about unit cell of a studied crystal structure.

The intensity I_{hkl} of the Bragg peaks, on the other hand, contains information about the atomic positions x_i, y_i, z_i in the unit cell as well as it provides information about occupancies O_i of atoms at the i^{th} position. This is expressed by the following formula [30]:

$$I_{hkl} \propto |F_{hkl}|^2, \quad (3)$$

and

$$F_{hkl} = \sum_i f_i O_i e^{2\pi i(hx_i + ky_i + lz_i)} \times e^{-\frac{B_i \sin^2 \theta}{\lambda^2}}$$

(4)

where f_i - atomic form factor of the i^{th} atom, O_i – occupancy of the i^{th} atom, F_{hkl} is a form factor, B_i is the isotropic thermal parameter, and the sum goes over all atoms in the unit cell.

2.2.1 X-ray powder diffraction

In the X-ray powder diffraction (XRPD) technique, the incident monochromatic X-ray beam hit the powder sample and the diffracted intensity is collected by a detector as a function of the diffraction angle 2θ . This type of the diffraction measurement is called a constant wavelength (CW) method.

In this study, the XRPD measurements for Ba_2MTaO_6 ($M = \text{Ce}, \text{Pr}$) and $\text{Ba}_3\text{Pr}_x\text{Ta}_y\text{O}_{9-\delta}$ ($x = 1, 2; y = 1, 2$) samples were carried out at room temperature using the Bruker[®] AXS D8 ADVANCE VARIO[®] powder diffractometer. The instrument was equipped with a copper anode (CuK_α radiation, $\lambda = 1.54056 \text{ \AA}$) and Ge (111) monochromator. Samples were loaded into a plastic sample holder. Later the sample was pressed into a flat surface. The measurement was carried out with a Lynx EyePSD[®] detector. The analysis of the raw data was carried out by using Bruker[®] AXS DIFFRACplus EVA[®] software combined with International center of diffraction database (ICDD).

2.2.2 Neutron powder diffraction

As a complementary method to XRPD, neutron powder diffraction (NPD) was used. Unlike X-rays, the scattering power of neutrons does not depend on the atomic number of elements. It depends only on the isotope composition of a material and is based on the nuclear interactions between neutrons and the atomic nuclei. In particular, neutron scattering is more sensitive for light elements as compared with XRPD. This makes the NPD technique very useful when it comes to study for instance, oxygen atomic positions and their occupancies.

The CW method, described earlier, can be used also for neutron scattering. However, in this work NPD was based on different approach, i.e. a polychromatic beam of neutrons is scattered on a sample and measured at the fixed 2θ position. According to Eq. 2, certain neutron wavelengths in the polychromatic beam will satisfy Bragg's condition and a detector will

record a signal as different d_{hkl} are scanned. Assuming a nonrelativistic relation $p = mv$, the neutron wavelength λ is related with its momentum by

$$\lambda = \frac{h}{mv}, \quad (5)$$

where m is the neutron mass and v its velocity. Knowing a distance L between a neutron source and a detector, Eq. 5 can be rewritten as

$$\lambda = \frac{h}{mv} = \frac{ht}{mL} \quad (6)$$

where t is time of flight of the neutrons. [31] As a final result on the measurement, a spectrum containing scattered neutron beam intensity as a function of the time of flight is obtained.

In this study, the time-of-flight (TOF) NPD was performed at the ISIS neutron facility, Rutherford Appleton Laboratory, UK on the high-resolution powder diffractometer (HRPD). Only $\text{Ba}_2\text{PrTaO}_6$ samples was analyzed. The sample was placed in an 8 mm-diameter cylindrical vanadium can. Because of the low flux of neutron, large amount of sample (typically no more than 5 g) is needed to reduce the counting times. Thus, it is possible to get good quality data within a reasonable time.

All measurements were performed at room temperature. Data were collected in three fixed 2 θ banks (30°, 90°, 168°). The exposure time for each sample was 5 h.

2.2.3 The Rietveld method

The diffraction data from both XRPD and TOF NPD measurements was analyzed using the Rietveld method [32]. In this method, simulated data y^{calc} is generated based on an initial structure model of a studied material. The calculated points are compared with the observed ones using a following functional

$$M = \sum_i W_i \left\{ y_i^{obs} - \frac{1}{c} y_i^{calc} \right\}^2,$$

(7)

where W_i is the statistical weight of a measured point (intensity) and c is the overall scale factor so that the $y^{calc} = cy^{obs}$. Using the iterative gradient methods, the final model parameters are obtained when M reaches a minimum.

Rietveld refinement in this thesis was done using the BRUKER® DIFFRAC.SUITE TOPAS® software.

2.3 Thermogravimetric analysis and differential scanning calorimetry

Thermogravimetric (TG) analysis measures the weight changes of a studied material as a function of temperature. Loss of water or decomposition of an organic compound leads to a weight loss. Absorption of gas as well as oxidation brings a gain in weight.

Differential scanning calorimetry (DSC) measures the energy differences compensated on both reference side and sample side. Energy needed to the sample side varies when a reaction or phase transition takes place. [6, 7]

In this thesis, a TG-DSC machine (Netzsch STA 409 PC Luxx®), as shown in Figure 2.2, was used for analyzing Ba_2CeTaO_6 and Ba_2PrTaO_6 . For a hydrated sample, the mass loss determined by TG-DSC indicates the amounts of protonic defects in the structure. Sample was placed in an alumina crucible. The temperature was increased by 25 °C/min up to 1000 °C. Nitrogen gas flux was used during the entire measurement.

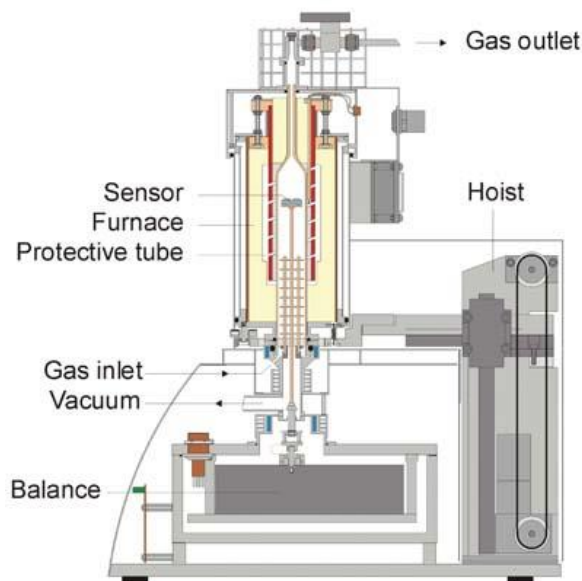


Figure 2.2 A brief description of TG-DSC machine setup.

2.4 Scanning electron microscopy and Energy dispersive spectroscopy

Scanning electron microscopy (SEM) is a common method to analyze the microstructure of materials. An electron beam created under certain potential is directed to the sample. The electrons hitting the atoms emits secondary electrons, back-scattered electrons, and characteristic X-rays. Secondary electrons are low energy electrons. Therefore, only those electrons close to the surface can be emitted as secondary electrons. Due to this, secondary electrons are sensitive to the surface. By collecting the secondary electrons, image of the material surface can be reconstructed.[6, 7]

The back-scattered electrons emitted by the incident beam have a high energy which varies with the atomic number. This selectivity allows for quantitative or qualitative measurements of a sample composition. The technique is called the energy dispersive spectroscopy (EDS).

In this study, SEM for $\text{Ba}_2\text{CeTaO}_6$ and $\text{Ba}_2\text{PrTaO}_6$ was done on LEO[®] Ultra 55 FEG SEM equipped with EDS from Oxford INCA.[®] Voltage for generating electrons was set at 30kV in order to get a better result on EDS.

2.5 Electrochemical impedance spectroscopy

Conductivity in crystallized oxide materials is defined by the diffusion of charge carriers between grain boundaries, grains and electrodes. When an alternating current (AC) voltage is applied on a material, electrical impedance will affect the diffusion of charge carriers. The impedance consists of three parts, which is the resistance, capacitance and inductance. Hence, the resistance is independent on the frequency of the AC voltage and capacitance and inductance are dependent on the frequency, which indicates that conductivity on bulk, grain boundary and electrode appears at different frequency. [6, 33, 34]

Impedance (Z) is described as a complex number

$$Z = Z' + iZ'' \tag{8}$$

where Z' is the real part of impedance, and Z'' is the imaginary part of the impedance that stands for the reactance, which is equal to L (Inductance) – C (Capacitance). As the frequency approaching zero, the Z' stands for the resistance. The impedance can be represented as a vector on the complex plane as shown in Figure 2.3.

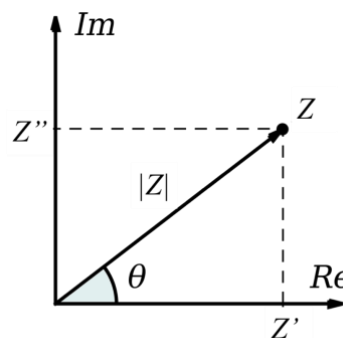


Figure 2.3 Representation of impedance on the complex plane.

Reactance varies with the frequency because of the capacitance and inductance. Impedance changes are recorded and plotted into a graph where Z' is against to Z'' (complex plane) as shown in Figure 2.4. Due to the frequency differences between bulk, grain boundary and electrode for conductivity, multiple semicircles can be found on the plot. One semicircle can

be simulated by a model containing a resistor and a constant phase element in parallel connection. However, due to the overlap of neighboring semicircles, it may become difficult to identify where the resistance is from. Capacitance can be used to determine the origin of resistance. In general, a bulk resistance will have the capacitance of around 10^{-12} F, a grain boundary resistance will have the capacitance between 10^{-11} to 10^{-8} F, and the electrode resistance will have the capacitance between 10^{-7} to 10^{-5} F. [6, 33, 34]

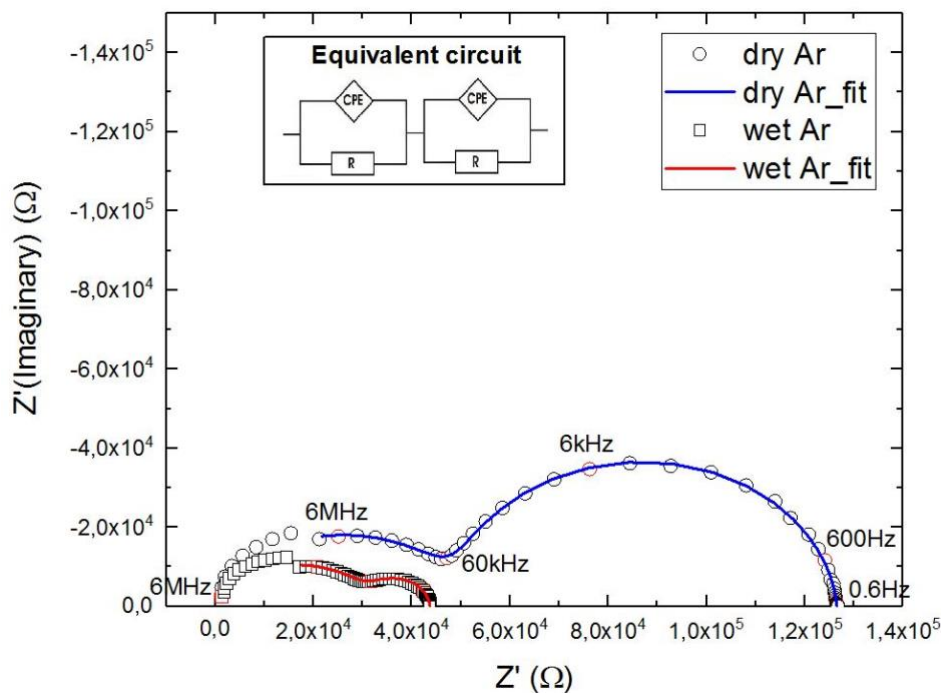


Figure 2.4 Impedance plot of BPT at 400°C under dry and wet Ar condition including the fitting of semicircles based on the model of equivalent circuit.

In this thesis, electrochemical impedance spectroscopy (EIS) was performed on a Probestat[®] (NorECs[®]) cell with the Solartron[®] 1260 analyzer for samples: Ba₂CeTaO₆, Ba₂PrTaO₆, and Ba₃PrTaO_{9-δ}. The description of the apparatus is shown in Figure 2.5. The potential applied on the sample was set at 1 V. Measurement was carried out under frequency varying from 6 MHz to 100 mHz. Temperature was set at 900 °C at first and cooled to 150 °C with each step for 50 °C. Different gas conditions (dry Ar, wet Ar, dry Air, wet Air, D₂O & Air) were applied during the measurement. Samples were prepared as 10 mm pellets and coated with Platinum paste (Metalor[®]) as electrode on both side. Zview[®] by Scribner Associate Inc.[®] software was

used to analyze the plot with the model shown in Figure 2.4. Conductivity σ was calculated using the equation:

$$\sigma(\text{Scm}^{-1}) = \frac{T(\text{cm})}{R(\Omega) \times A(\text{cm}^2)}, \quad (9)$$

where T is the thickness of the pellet, R is the resistance, and A is the area of the platinum electrode. The results of the EIS measurements can be shown as a so-called Arrhenius plot which presents $\log \sigma$ against $1000/T$. Arrhenius equation is written as:

$$\sigma = \sigma_o e^{\frac{-E_a}{RT}}, \quad (10)$$

where σ_o is a constant, R is the gas constant, T is the temperature in kelvin, and E_a is the activation energy. Eq. 10 can be rewritten by taking the logarithm on both side of the equation as follows;

$$\log \sigma = -\frac{E_a}{R} \times \frac{1}{T} + \log \sigma_o \quad (11)$$

Arrhenius equation was established on an empirical relationship, which makes it possible to be used on all thermal-induced processes, such as the conductivity dependence on temperature. By plotting the data with $\log \sigma$ against $1/T$, the slop of the fitted line can be used to calculate the activation energy.

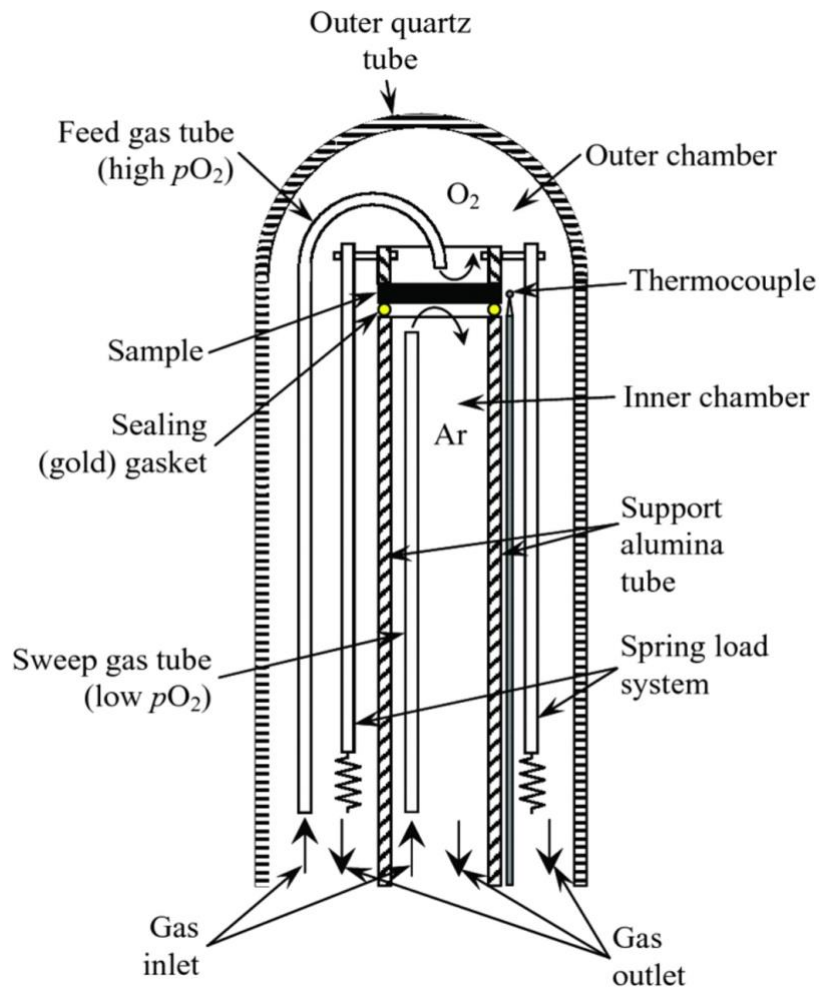


Figure 2.5 Description of the cell setup used for the impedance measurements.

3 Result and Discussion

3.1 Diffraction

XRPD data collected from the following samples, $\text{Ba}_2\text{CeTaO}_6$ (BCT), $\text{Ba}_2\text{PrTaO}_6$ (BPT), $\text{Ba}_3\text{Pr}_2\text{TaO}_{9-\delta}$ (B3P2T), $\text{Ba}_3\text{PrTa}_2\text{O}_{9-\delta}$ (B3PT2) and $\text{Ba}_3\text{PrTaO}_{9-\delta}$ (B3PT), was analyzed. Furthermore, TOF NPD data for the $\text{Ba}_2\text{PrTaO}_6$ sample was analyzed. From Figure 3.1, one can see that, compared to the ICDD database, the phase BCT was pure after synthesis at the maximum temperature of 1425 °C. From the Rietveld Refinement, a monoclinic structure could be confirmed, as shown in Figure 3.2. The detailed crystallographic data is shown in Table 3.1 However, due to the limitation of X-ray diffraction, it was not possible to refine the atomic positions and occupancies in the structure, which is reflected in a relatively poor fit.

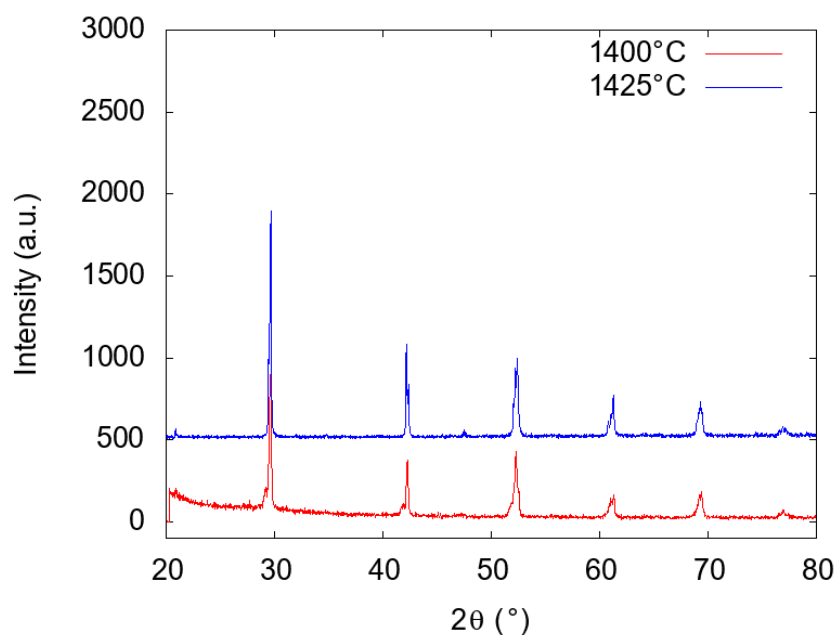


Figure 3.1 XRPD patterns of BCT synthesized at 1400 °C and 1425 °C.

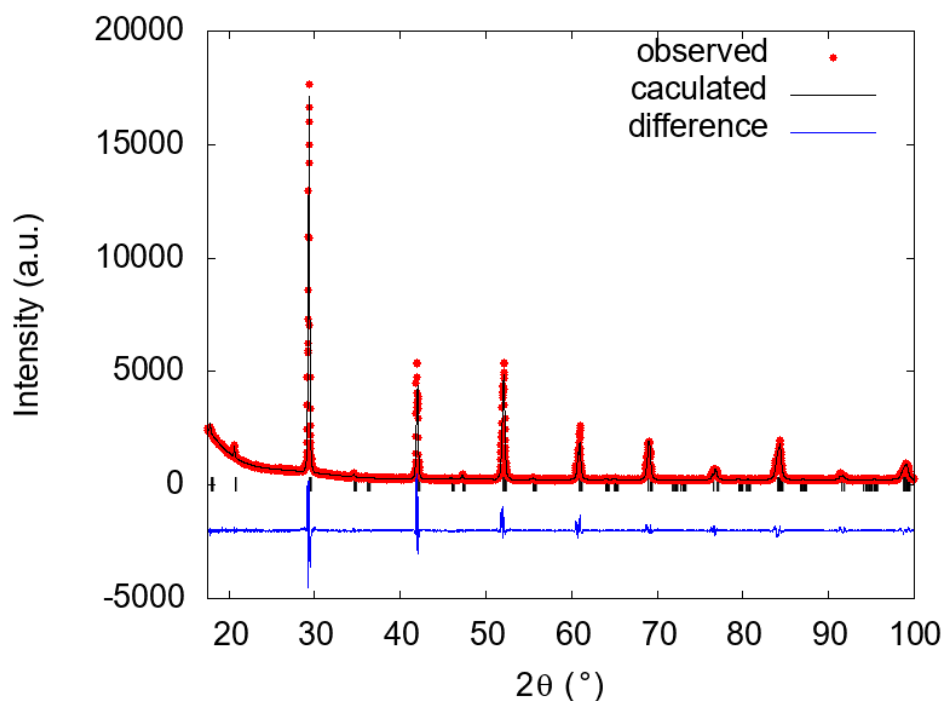


Figure 3.2 Rietveld refinement on XRPD for BCT.

Table 3.1 Crystallographic data for the BCT structure after Rietveld refinement.

Sample	Ba ₂ CeTaO ₆	Space group	<i>I</i> 2/m
Instrument	Bruker® AXS D8 ADVANCE VARIO®	a (Å)	6.0781(1)
Wavelength (Å)	1.54056	b (Å)	6.0679(1)
2θ range (°)	15° to 100°	c (Å)	8.6125(1)
Step size (°)	0.0144	β (°)	90.3033(4)
R _p	7.13	R _{exp}	4.41
R _{wp}	10.78	GOF	2.45

Figure 3.3 shows the XRPD pattern for BPT under different steps of treatment while sintering. At 1350 °C, compared to the similar structure BCT, the pattern is well fitted into a monoclinic structure. This indicates that a pure phase was achieved. BPT is a material that has never been reported in the ICSD database. In this case, the TOF NPD data was used for the Rietveld analysis. The structure of BCT was used as a starting model. The Rietveld refinement showed that BPT crystallize in a monoclinic system. The structure is well fitted with space group $I2/m$. Figure 3.4 shows the result of Rietveld refinement on TOF data. The refinement parameters are summarized in Table 3.3 and Table 3.4. Occupancy of the oxygen atoms was close to 1 and therefore for the final refinement were fixed to 1. A structure based on the refinement result is shown in Figure 3.5 and it indicates a double perovskite structure. Some selected bond distances are shown in Table 3.5. Compared to the crystallographic data of BCT from Zhou [35] shown in Table 3.2, the Ba-O bond distance and the Ta-O bond distance in BPT are reasonably close to the corresponding bond in BCT. Structural refinement of BCT from the ICDD database is based on only X-ray data, which lower the precision and may become an explanation of that tiny difference. Pr-O bond distance is smaller than the Ce-O bond, because Pr³⁺ (0.99 Å) shows smaller ionic radii than Ce³⁺ (1.01 Å) in 6 coordination. Thus, the tilting of octahedra in BPT will be less than in BCT, which indicate a β closer to 90° and slightly smaller a , b , c . It can be confirmed by calculating the tolerance factor for both. The BPT shows slightly larger tolerance factor than BCT.

Table 3.2 Selected bond distances for BCT from ICSD database. [35]

Bond	Distance (Å)
Ba—O(1) × 1	2.75(2)
Ba—O(1) × 2	3.08(1)
Ba—O(1) × 1	3.39(2)
Ba—O(2) × 2	2.83(2)
Ba—O(2) × 2	2.92(1)
Ba—O(2) × 2	3.16(2)
Ba—O(2) × 2	3.27(2)
Ce—O(1)	2.46(2)
Ce—O(2)	2.35(2)
Ta—O(1)	1.89(2)
Ta—O(2)	1.97(2)

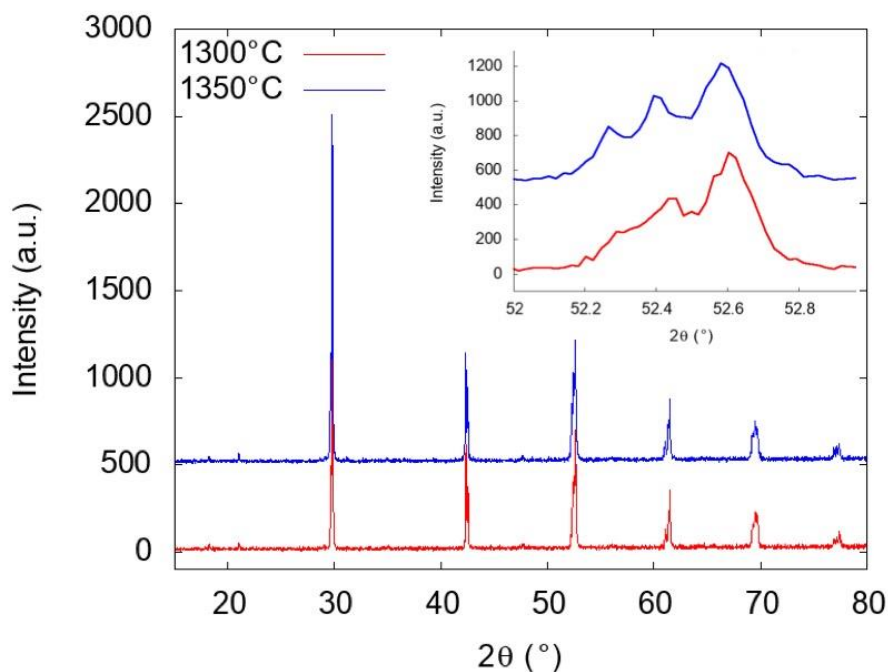


Figure 3.3 XRPD patterns of BPT synthesized at 1300 °C and 1350 °C. The insert shows a better crystallinity for the sample annealed at 1350 °C.

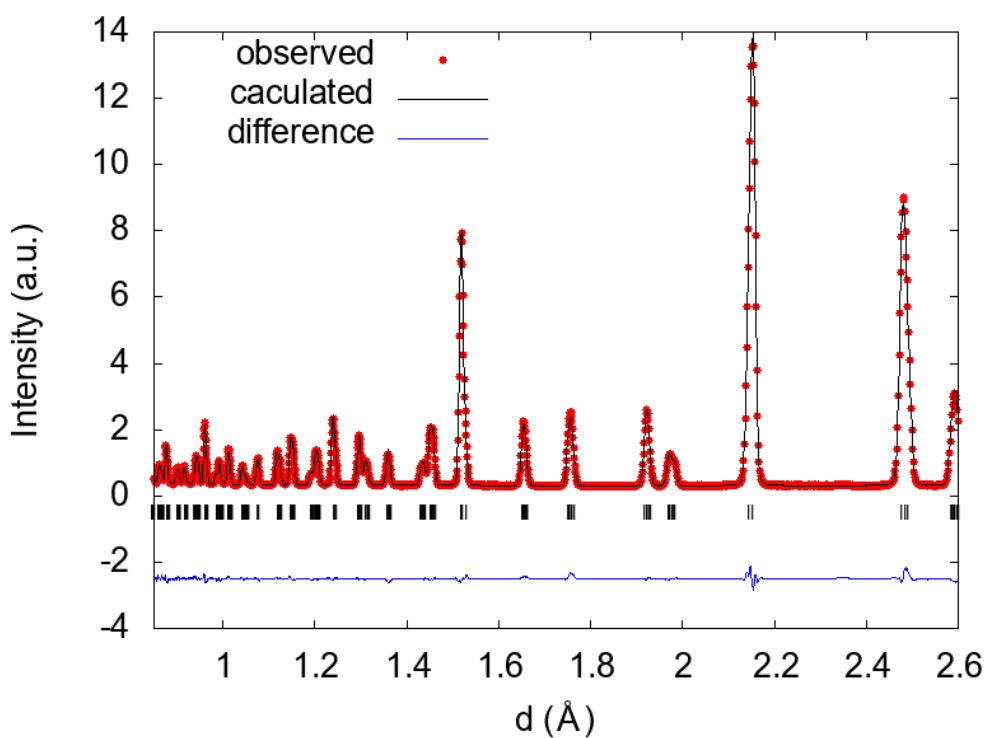


Figure 3.4 Rietveld Refinement on HRPD data from the 168° detector bank for BPT.

Table 3.3 crystallographic data for BPT structure after Rietveld refinement.

Sample	Ba ₂ PrTaO ₆	Space group	<i>I</i> 2/m
Instrument	HRPD	a (Å)	6.1004(2)
		b (Å)	6.0618(2)
2θ banks (°)	30°, 90°, 168°	c (Å)	8.5617(3)
d-spacing range(Å)	0.65 to 10.20	β (°)	90.1815(5)
R _p	5.23	R _{exp}	1.53
R _{wp}	3.75	GOF	2.45

Table 3.4 Atomic positions, occupancies and displacements for BPT after Rietveld refinement.

Atom	Site	<i>x</i>	<i>y</i>	<i>z</i>	Occ.	<i>B</i> _{iso}
Ba	4i	0.5023(2)	0	0.2482(1)	1	0.76(1)
Pr	2a	0	0	0	1	0.83(1)
Ta	2d	1/2	1/2	0	1	0.21(1)
O(1)	4i	0.0541(1)	0	0.2699(1)	1	1.08(1)
O(2)	8j	0.2711(1)	0.2670(1)	-0.0285(1)	1	1.41(1)

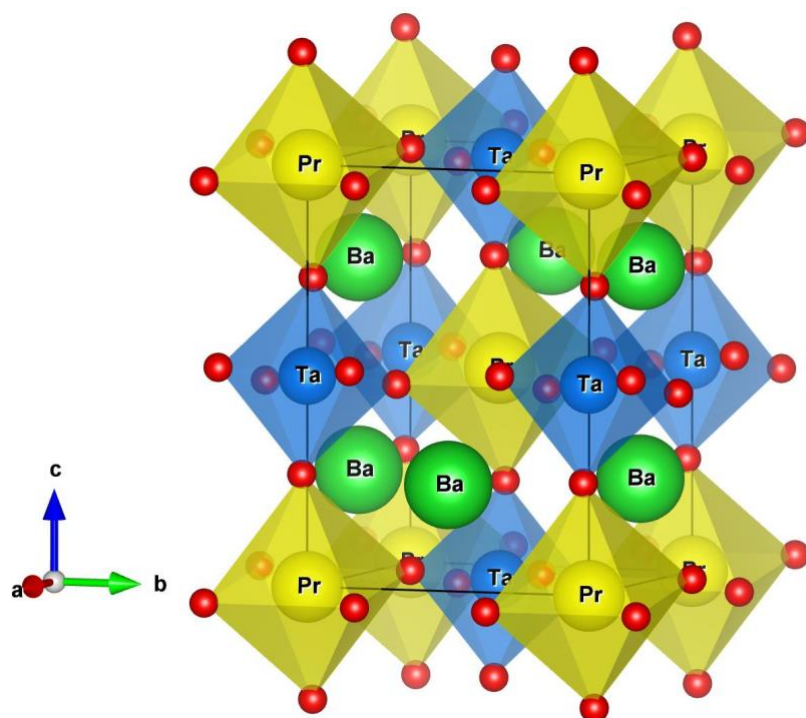


Figure 3.5 Refined structure of BPT.

Table 3.5 Selected bond distances for BPT after Rietveld refinement.

Bond	Distance (Å)
Ba — O(1) × 1	2.74(1)
Ba — O(1) × 2	3.05(1)
Ba — O(1) × 1	3.37(1)
Ba — O(2) × 2	2.84(1)
Ba — O(2) × 2	2.88(1)
Ba — O(2) × 2	3.19(1)
Ba — O(2) × 2	3.25(1)
Pr — O(1)	2.33(1)

Pr — O(2)	2.33(1)
Ta — O(1)	2.00(1)
Ta — O(2)	2.00(1)

Figure 3.6 shows the XRPD results of the $\text{Ba}_3\text{Pr}_x\text{Ta}_y\text{O}_{9-\delta}$ series, which clearly shows the possibility of synthesizing B3PT in pure form as there are no sign of impurity peaks. Solid state synthesis is limited by the diffusion through the formed product. A homogeneous mixture of reactants in correct cation ratio will minimize diffusion paths and, in this case, formed the desired compound with respect to composition.

However, the attempt to prepare pure B3PT2 and B3P2T samples were not completely successful by the solid-state synthesis route. In order to overcome this obstacle, the plan is to use a solution route to prepare those materials, either by direct precipitation from solution or by a “sol-gel” route. See a review by Kakihana [36] and references therein. The mixing on an atomic level becomes much better and therefor the diffusion paths are minimized. This leads to much shorter reaction times. In addition, final sintering temperatures can be dramatically reduced, which also make it possible to form phases not stable at elevated temperatures. Related compounds, like many complex high- T_c superconductors or high melting point ceramics, have been prepared by different polymerized complex methods [37-40]. These preparative routes will be tried for synthesis of pure B3PT2 and B3P2T compounds.

Finally, B3PT, shown in Figure 3.6, is a new material, never mentioned in a data base. As shown in Figure 3.7, all diffraction peaks can be indexed, and lattice parameters refined using the Pawley method within space group $P2/m$. Then pattern matching shown in Figure 3.7 strongly indicates a single phase sample (see Table 3.6). Structure solution, however, is not possible with the XRPD data and it is planned in the future.

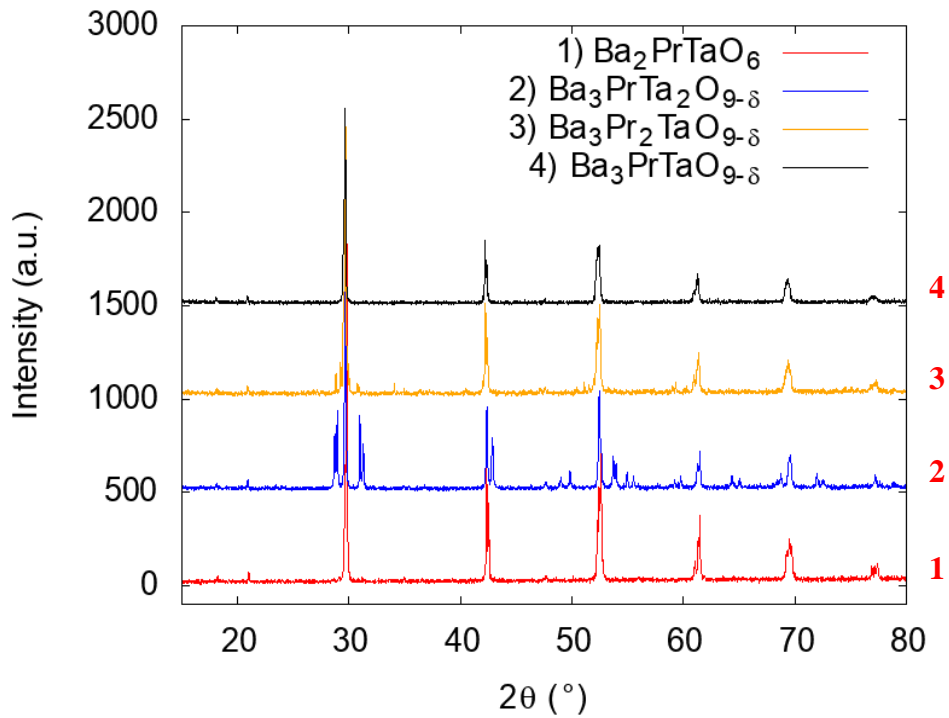


Figure 3.6 XRPD patterns of $\text{Ba}_3\text{Pr}_x\text{Ta}_y\text{O}_{9-\delta}$. The patterns are compared with a phase pure $\text{Ba}_2\text{PrTaO}_6$ to examine the purity.

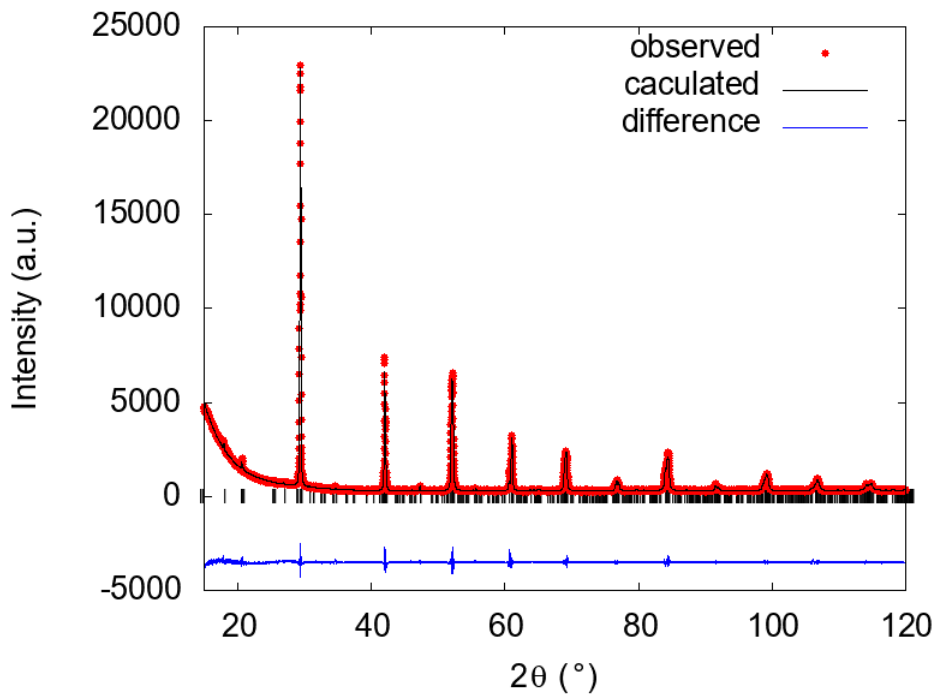


Figure 3.7 Pattern matching of $\text{Ba}_3\text{PrTaO}_{9-\delta}$ using the Pawley method.

Table 3.6 crystallographic data for B3PT structure after Pawley refinement.

Sample	Ba ₃ PrTaO _{9-δ}	Space group	<i>P2/m</i>
Instrument	Bruker® AXS D8 ADVANCE VARIO®	a (Å)	6.5913(5)
Wavelength (Å)	1.54056	b (Å)	6.0389(5)
2θ range (°)	15° to 120°	c (Å)	9.1090(4)
Step size (°)	0.0144	β (Å)	110.954(3)
R _p	4.44	R _{exp}	3.77
R _{wp}	6.79	GOF	1.80

3.2 Scanning electron microscopy and Energy dispersive spectroscopy

Figure 3.8 and Figure 3.9 show SEM micrographs. For BCT, there are some particles on the surface that was not densified. However, beneath the dispersed particles, it is an almost fully dense layer with only limited porosity. The overall particle size is around 4 μm. For BPT, there is no dispersed particles on the surface as in BCT. Densification of the pellet is satisfactory with only few pores shown on Figure 3.9. The overall particle size is around 2 μm. With the picture taken above, the atom percentages of each elements were measured by EDS, shown in Table 3.7. Both the Ba:(Ce/Pr +Ta) ratio was around 1.07:1, which is close to the theoretical formula (within experimental error). Besides Ba, the ratio between Ce/Pr and Ta was 1.15:1 and 1.14:1. However in the theoretical formula, Ce/Pr to Ta should have a 1:1 ratio. The divergence between EDS result and theoretical result occur because different condition used for measurement and calibration. The correction file used was based on a highly polished (metal) standard. However, for measurement of the complex ceramic oxides it was not possible to obtain such a smooth highly-polished surface as with the standard used.

A highly accurate EDS result is only given when the standard sample and the investigated sample are measured under very similar condition such as the electron gun used, the same position related to the beam and the detector, the level of surface polishing, the thickness of the sample and etc., which is not always possible when carrying out an experiment. Based on Goldstein's summary [41], most of the EDS result gave $\pm 25\%$ of deviation to the theoretical result.

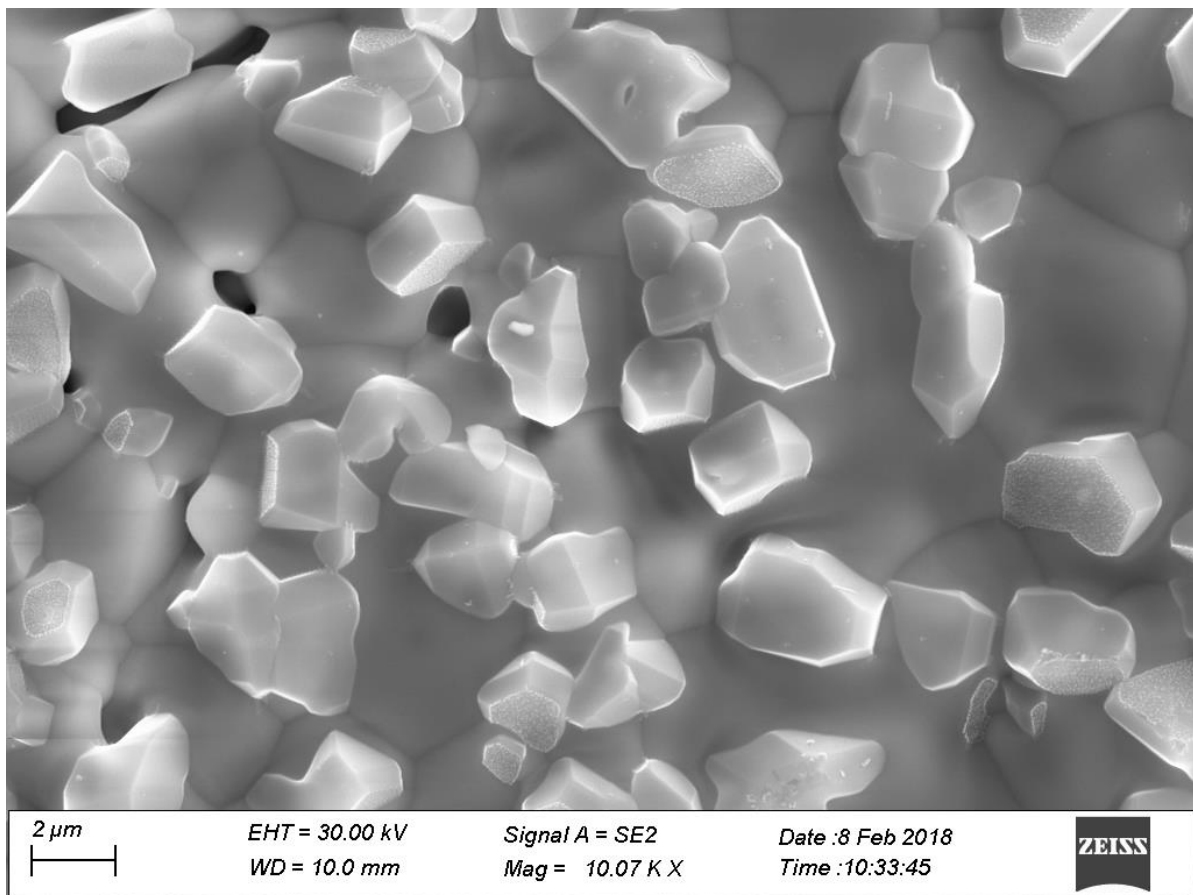


Figure 3.8 SEM micrograph of the BCT pellet.

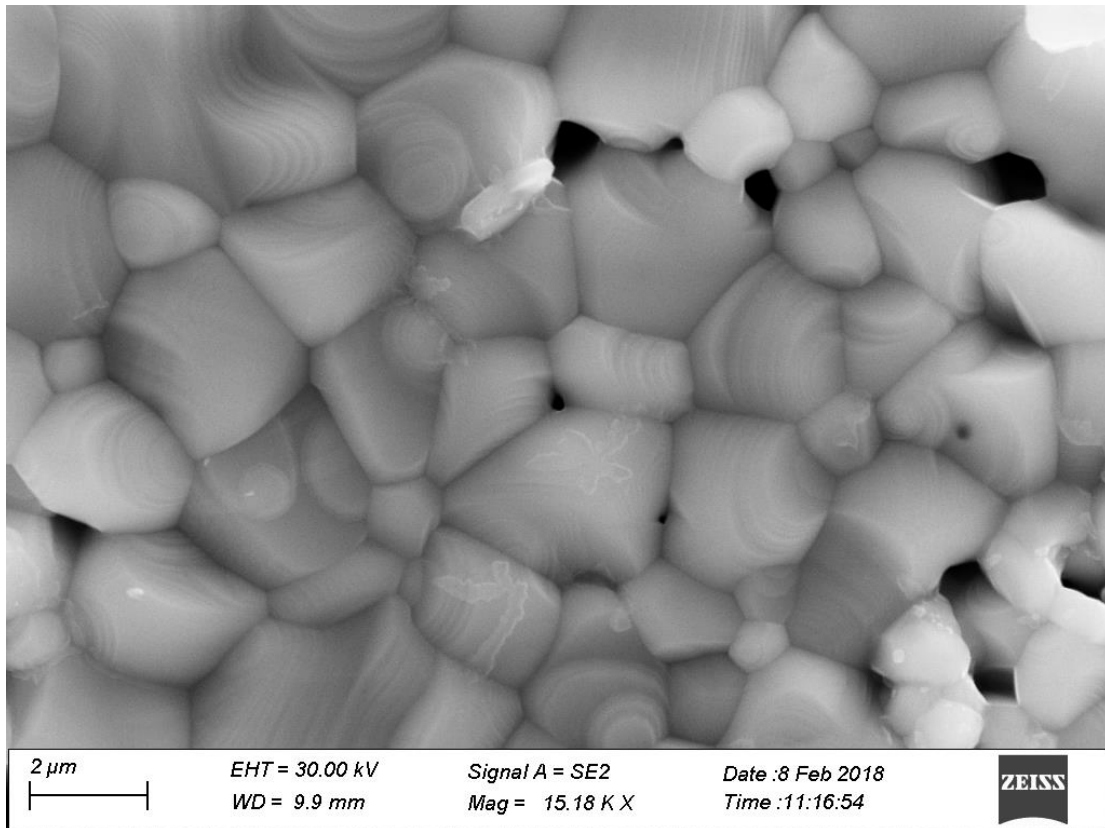


Figure 3.9 SEM micrograph of the BPT pellet.

Table 3.7 EDS result for BCT and BPT pellet.

Site	Ba%	Ce%	Ta%
1	51.27	22.91	25.82
2	50.59	22.77	26.64
3	52.21	21.98	25.81
4	51.84	22.42	25.74
Average	51.48	22.52	26.00

Site	Ba%	Pr%	Ta%
1	51.73	22.25	26.02
2	51.69	22.52	25.79
3	51.70	22.67	25.63
4	51.86	22.60	25.54
Average	51.75	22.51	25.75

3.3 Thermogravimetric analysis and differential scanning calorimetry

Figure 3.10 and Figure 3.11 show the TG-DSC result from BCT and BPT. Samples were hydrated at the temperature from 600 °C to 150 °C. For both samples, there is no mass change on the TG signal, which indicates no dehydration process occurred during the measurement. On the DSC signal, also do not show any significant endothermic peak. However, dehydration is an endothermic reaction, which will have a positive peak at a certain temperature when the reaction happens. In general, based on the result from TG and DSC, we can conclude that there are not enough oxygen vacancies on the synthesized samples (as prepared BCT or BPT). In addition, the Rietveld refinement on neutron powder diffraction data on BPT sample also confirms the absence of oxygen vacancies. Samples containing impurities were not further analyzed for TG-DSC. Concerning the B3PT sample, TG-DSC data has not yet been collected but measurements are planned.

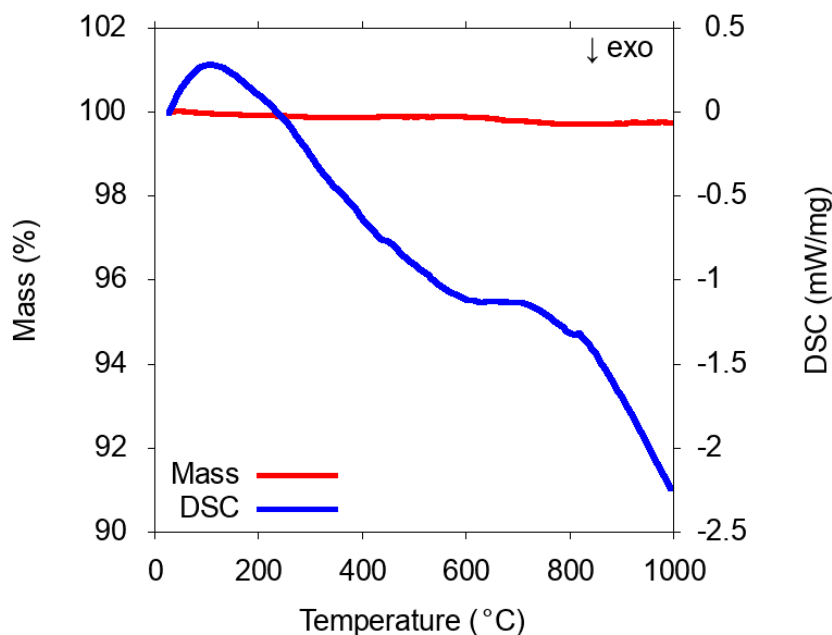


Figure 3.10 TG-DSC for hydrated BCT under inert atmosphere.

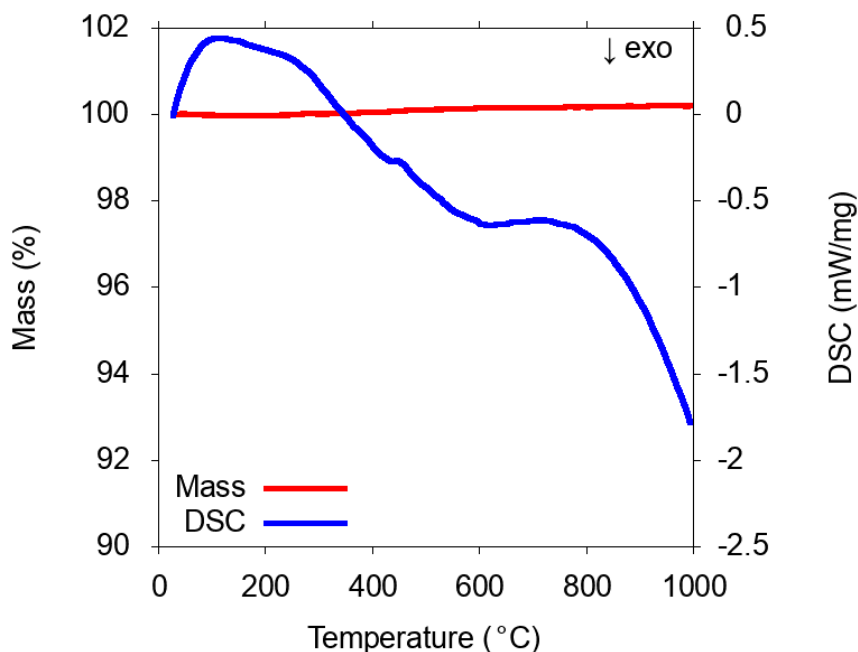


Figure 3.11 TG-DSC for hydrated BPT under inert atmosphere.

3.4 Electrochemical characterization

Figure 3.12, Figure 3.13 and Figure 3.14 show the Arrhenius plots of BCT, BPT and B3PT where $\log \sigma$ is plotted against $1000/T$. Samples for measurement might be hydrated during the synthesis or storage so that the heating cycle initially was used to fully dehydrate the samples. Data presented here in the plot was made during the cooling cycle. Samples with impurities as B3P2T and B3PT2 were not analyzed with respect to conductivity. From Figure 3.12, the total conductivity under dry Ar, as well as the activation energy, is higher than wet Ar. Especially at high temperature, a big increase on total conductivity occurred. However, a proton conductor would have a better conductivity at higher humidity because of more protons involved. Total conductivity under dry Ar and dry Air also shows a big decrease especially at high temperature, which indicates no hopping conductivity. In general, the Arrhenius plot of BCT do not indicate any proton or ionic conductivity.

For BPT, shown in Figure 3.13, a proton conductivity seems to appear, especially at the range from 400 °C to 900 °C. Comparing the total conductivity under dry Ar with wet Ar, we can see in the wet condition, the total conductivity is much higher (1/2 order of magnitude). This is an indication of the presence of proton conductivity around 150 °C to 850 °C. An

explanation for this is more protons will be involved at higher humidity, which indicate more charge carriers and also lower activation energy. Further measurement under wet D₂O, Ar condition shows a slight decrease in conductivity from 150 °C to 850 °C, where $\frac{\sigma_H}{\sigma_o} = 1.16$ and $\Delta E = E_H - E_D = 0.02$ eV, which is due to the isotope effect. According to the report from Nowick et al [42], proton conductivity of perovskite structure from an Arrhenius plot shows a difference of activation energy around 0.03 eV to 0.06 eV by substitution of Deuterium for Hydrogen. Although, TG results suggests, these sample do not hydrate. The possible explanation of this higher conductivity can be from interstitial protons under dynamic humid condition. However, further investigation is needed to explain this behavior. Total conductivity under more oxidizing conditions shows a higher conductivity above 150 °C. With more oxygen, hopping conductivity will occur and make the praseodymium atoms transfer between Pr³⁺ and Pr⁴⁺. This indicates a p-type semiconductor.

At 400 °C, BPT has a total conductivity for 4.27×10^{-5} Scm⁻¹ under wet Ar, which shows better total conductivity compared to BaTi_{0.8}Sc_{0.2}O_{3- δ} with a total conductivity for 2.61×10^{-6} Scm⁻¹ [43]. However, compared to the most studied Ba₃Ca_{1.18}Nb_{1.82}O_{9- δ} (BCN18), BCN18 has a total conductivity for 2×10^{-4} Scm⁻¹ at 200 °C under wet Ar [44], where BPT has a lower total conductivity for 4.6×10^{-7} Scm⁻¹. It is not surprising because of the absence of oxygen vacancies in BPT.

In Figure 3.14, the Arrhenius plot shows a slightly decreased conductivity from dry Ar to wet Ar, which indicates no proton conductivity in B3PT. But under either dry or wet condition, with more oxygen content, the total conductivity is increased at 200 °C up to 350 °C, which indicates existence of electronic conductivity.

Further investigation on bulk conductivity and boundary conductivity has not been analyzed.

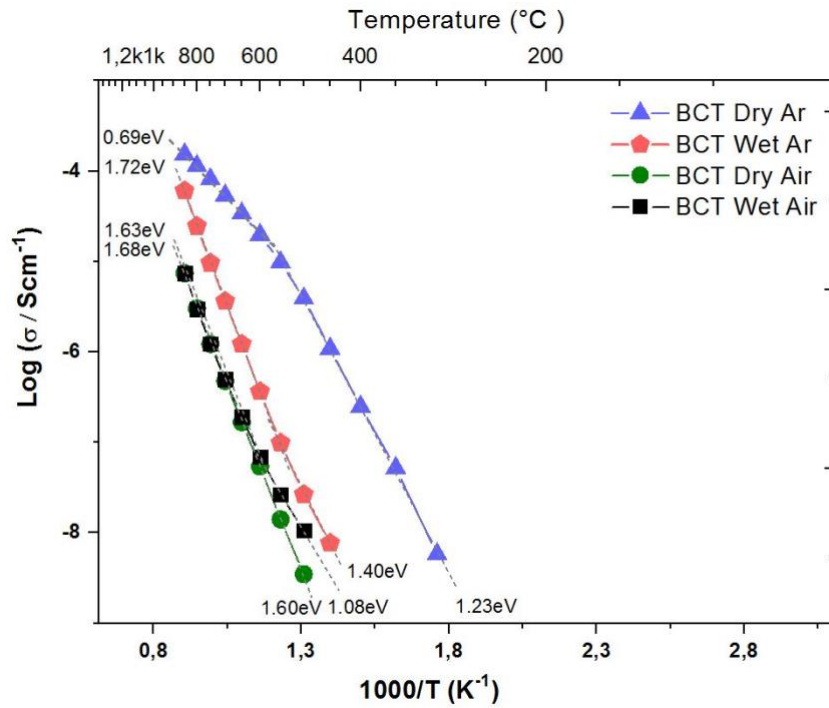


Figure 3.12 Arrhenius plot for the total conductivity of BCT measured under different conditions.

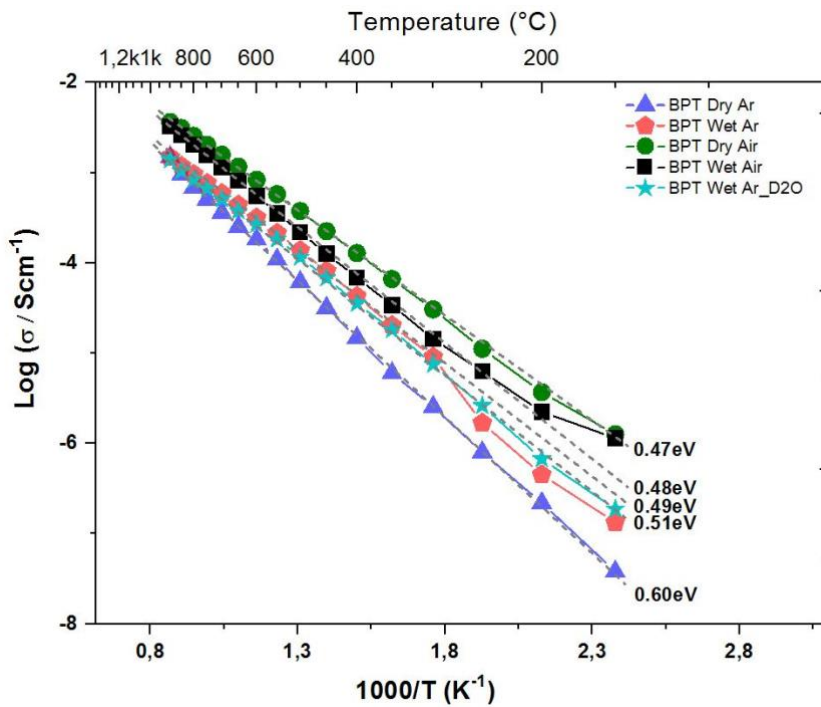


Figure 3.13 Arrhenius plot for the total conductivity of BPT measured under different conditions.

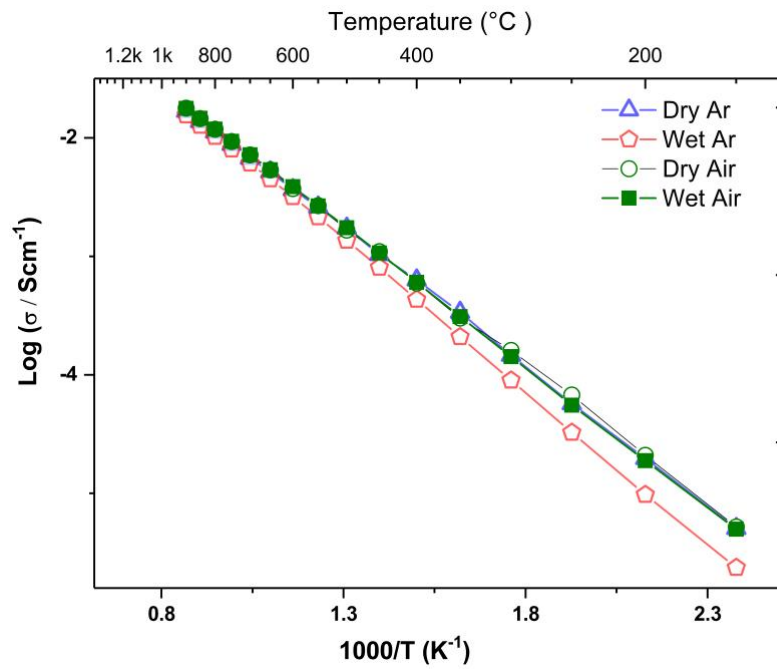


Figure 3.14 Arrhenius plot for the total conductivity of B3PT measured under different conditions

4 Conclusion

Conductivity of a series of complex perovskite oxides was studied in this thesis. Solid-state synthesis method was used to synthesize the samples. BCT, BPT and $\text{Ba}_3\text{Pr}_x\text{Ta}_y\text{O}_{9-\delta}$ series has been synthesized but only BCT, BPT, and B3PT were pure phases shown in Figure 3.2, Figure 3.4 and Figure 3.7. Figure 3.7 also indicates that, for $\text{Ba}_3\text{Pr}_x\text{Ta}_y\text{O}_{9-\delta}$ series, it is possible to synthesize pure sample when x and y are below 1.5. Microwave assisted hydrothermal synthesis can be a way to synthesize pure sample when x and y are above 1.5. Rietveld refinement with the TOF NPD data for BPT showed a monoclinic structure with a space group $I2/m$. Further investigation on the structure of other $\text{Ba}_3\text{Pr}_x\text{Ta}_y\text{O}_{9-\delta}$ series samples by using neutron powder diffraction will be interesting and is planned in the future. It would also be interesting to compare the difference on particle size by using microwave assisted hydrothermal synthesis method and solid-state synthesis method. No oxygen vacancy was found in BPT as TG-DSC data, shown in Figure 3.11, and Rietveld refinement results, shown in Figure 3.4, both confirmed the result. At the intermediate temperature range, BPT showed the best conductivity in this study, shown in Figure 3.12. Compared to the latest result on proton conducting materials, it does not show an outstanding proton conductivity. However, BPT not only showed proton conductivity but also electronic conductivity. It can be predicted that with more oxygen vacancies created, it may be a good candidate as cathode material in PCFC. Further investigation on how the electronic conductivity for BPT will behave will also become interesting. Proton conductivity in BPT needs further investigation on the mechanism.

5 Bibliography

1. Steele, B.C. and A. Heinzl, *Materials for fuel-cell technologies*, in *Materials For Sustainable Energy: A Collection of Peer-Reviewed Research and Review Articles from Nature Publishing Group*. 2011, World Scientific. p. 224-231.
2. Stambouli, A.B. and E. Traversa, *Solid oxide fuel cells (SOFCs): a review of an environmentally clean and efficient source of energy*. *Renewable and sustainable energy reviews*, 2002. **6**(5): p. 433-455.
3. Fabbri, E., et al., *Towards the Next Generation of Solid Oxide Fuel Cells Operating Below 600° C with Chemically Stable Proton-Conducting Electrolytes*. *Advanced materials*, 2012. **24**(2): p. 195-208.
4. Boaro, M., et al., *Advances in Medium and High Temperature Solid Oxide Fuel Cell Technology*. Vol. 574. 2017, Cham: Springer International Publishing.
5. Azad, A.K., *Synthesis, structure, and magnetic properties of double perovskites of the type A_2MnBO_6 and A_2FeBO_6 ; (A= Ca, Sr, Ba, La; B= W, Mo, Cr)*. 2004.
6. Rahman, S., *Synthesis, Structure and Proton Conduction of Substituted $BaTiO_3$ and $BaZrO_3$ Perovskites*. 2013: Chalmers University of Technology.
7. Smart, L. and E. Moore, *Solid state chemistry: an introduction*. Vol. 4. 2012, Boca Raton: CRC Press.
8. Fabbri, E., D. Pergolesi, and E. Traversa, *Electrode materials: a challenge for the exploitation of protonic solid oxide fuel cells*. *Science and technology of advanced materials*, 2010. **11**(4): p. 044301.
9. Kwon, O.H. and G.M. Choi, *Electrical conductivity of thick film YSZ*. *Solid State Ionics*, 2006. **177**(35-36): p. 3057-3062.
10. Steele, B., *Material science and engineering: the enabling technology for the commercialisation of fuel cell systems*. *Journal of Materials Science*, 2001. **36**(5): p. 1053-1068.
11. Brett, D.J., et al., *Intermediate temperature solid oxide fuel cells*. *Chemical Society Reviews*, 2008. **37**(8): p. 1568-1578.
12. Iwahara, H., et al., *Proton conduction in sintered oxides and its application to steam electrolysis for hydrogen production*. *Solid State Ionics*, 1981. **3**: p. 359-363.
13. Liang, K. and A. Nowick, *High-temperature protonic conduction in mixed perovskite ceramics*. *Solid State Ionics*, 1993. **61**(1-3): p. 77-81.

14. Du, Y. and A. Nowick, *Galvanic cell measurements on a fast proton conducting complex perovskite electrolyte*. Solid State Ionics, 1996. **91**(1-2): p. 85-91.
15. Bhella, S.S. and V. Thangadurai, *Synthesis and characterization of carbon dioxide and boiling water stable proton conducting double perovskite-type metal oxides*. Journal of Power Sources, 2009. **186**(2): p. 311-319.
16. Fabbri, E., et al., *Chemically Stable Pr and Y Co-Doped Barium Zirconate Electrolytes with High Proton Conductivity for Intermediate-Temperature Solid Oxide Fuel Cells*. Advanced Functional Materials, 2011. **21**(1): p. 158-166.
17. Furuichi, S., et al., *Ion Conduction of BaPrO_{3-δ} Thin Film with Mixed Valence State for SOFC Anode Electrode*. ECS Transactions, 2017. **75**(42): p. 99-103.
18. Haugrud, R. and T. Norby, *Proton conduction in rare-earth ortho-niobates and ortho-tantalates*. Nature Materials, 2006. **5**(3): p. 193.
19. Goldschmidt, V., *Skrifter utgitt av det Norske Videnskaps-Akademi*. I Oslo, 1926. **1**.
20. Shannon, R.D., *Revised effective ionic radii and systematic studies of interatomic distances in halides and chalcogenides*. Acta crystallographica section A: crystal physics, diffraction, theoretical and general crystallography, 1976. **32**(5): p. 751-767.
21. Rahman, S.H., *Search for New Proton Conductors in Complex Perovskite Oxides*. 2007: Chalmers University of Technology.
22. Souza, E.C.C.d. and R. Muccillo, *Properties and applications of perovskite proton conductors*. Materials Research, 2010. **13**: p. 385-394.
23. Kreuer, K., *Aspects of the formation and mobility of protonic charge carriers and the stability of perovskite-type oxides*. Solid State Ionics, 1999. **125**(1-4): p. 285-302.
24. Kreuer, K.-D., A. Rabenau, and W. Weppner, *Vehicle Mechanism, A New Model for the Interpretation of the Conductivity of Fast Proton Conductors*. Angewandte Chemie International Edition in English, 1982. **21**(3): p. 208-209.
25. Weller, M.T., *Inorganic materials chemistry*. 1994: Oxford University Press.
26. Tilley, R.J., *Principles and applications of chemical defects*. 1998: CRC Press.
27. Pfleeger, R.L. and L. Mandel, *Interference of independent photon beams*. Physical Review, 1967. **159**(5): p. 1084.
28. Bragg, W.H. and W.L. Bragg. *The structure of the diamond*. in *Proc. R. Soc. Lond. A*. 1913. The Royal Society.
29. Weller, M.T. and N.A. Young, *Characterisation Methods in Inorganic Chemistry*. 2017: Oxford University Press.

30. Glusker, J.P. and K.N. Trueblood, *Crystal structure analysis: a primer*. Vol. 14. 2010: Oxford University Press.
31. Ibberson, R., W. David, and K. Knight, *The high resolution powder diffractometer (HRPD) at ISIS-a user guide*. 1992.
32. Rietveld, H., *A profile refinement method for nuclear and magnetic structures*. Journal of applied Crystallography, 1969. **2**(2): p. 65-71.
33. Kinyanjui, F.G., *Functional Oxide Materials exhibiting Ionic Conductivity for Future Energy Conversion Needs*. 2013: Chalmers University of Technology.
34. Barsukov, Y. and J.R. Macdonald, *Electrochemical impedance spectroscopy. Characterization of materials*, 2012.
35. Zhou, Q., et al., *Synthesis, Structural and Magnetic Studies of the Double Perovskites $Ba_2Ce M O_6$ ($M = Ta, Nb$)*. Chemistry of Materials, 2012. **24**(15): p. 2978-2986.
36. Kakihana, M., *Invited review "sol-gel" preparation of high temperature superconducting oxides*. Journal of Sol-Gel Science and Technology, 1996. **6**(1): p. 7-55.
37. KAKIHANA, M., et al., *Chemical Design for Functional Multi-Component Oxides by Polymerized Complex Method*, in *Advanced Materials' 93, I*. 1994, Elsevier. p. 801-806.
38. Kakihana, M., et al., *Fabrication and characterization of highly pure and homogeneous $YBa_2Cu_3O_7$ superconductors from sol-gel derived powders*. Journal of applied physics, 1991. **69**(2): p. 867-873.
39. Kakihana, M., et al., *Raman spectra, superconductivity, and structure of Co-substituted $YBa_2Cu_3O_{7-\delta}$* . Physical Review B, 1989. **40**(10): p. 6787.
40. Kakihana, M., et al., *High-quality ceramics of $YBa_2Cu_4O_8$ from citrate sol-gel precursors sintered at one atmosphere oxygen pressure*. Physica C: Superconductivity, 1991. **173**(5-6): p. 377-380.
41. Goldstein, J.I., et al., *Scanning electron microscopy and X-ray microanalysis*. 2017: Springer.
42. Nowick, A. and A. Vaysleyb, *Isotope effect and proton hopping in high-temperature protonic conductors*. Solid State Ionics, 1997. **97**(1-4): p. 17-26.
43. Rahman, S.M., et al., *Proton conductivity of hexagonal and cubic $BaTi_{1-x}Sc_xO_{3-\delta}$ ($0.1 \leq x \leq 0.8$)*. Dalton Transactions, 2014. **43**(40): p. 15055-15064.
44. Schober, T., F. Krug, and W. Schilling, *Criteria for the application of high temperature proton conductors in SOFCs*. Solid State Ionics, 1997. **97**(1-4): p. 369-373.

